Supporting Information for

"Band-Gap Deformation Potential and Elasticity Limit of Semiconductor Free-Standing Nanorods Characterized *in-Situ* by Scanning Electron Microscope-Cathodoluminescence Nanospectroscopy"

Kentaro Watanabe[*,1,2], Takahiro Nagata[1], Yutaka Wakayama[1], Takashi Sekiguchi[1], Róbert Erdélyi[3], and János Volk[3]

[1]WPI Center for Materials Nanoarchitectonics, National Institute for Materials Science, 1-1 Namiki, Tsukuba, Ibaraki 305-0044, Japan
[2]Faculty of Pure and Applied Sciences, University of Tsukuba, 1-1-1 Tennodai, Tsukuba, Ibaraki 305-8571, Japan
[3]MTA EK Institute of Technical Physics and Materials Science, 1121 Budapest, Konkoly Thege M. út 29-33., Hungary

[*]Electronic mail: WATANABE.Kentaro@nims.go.jp

Supplementary Note 1

Possible a_{cc} errors due to the conventional static ZnO NW bending

The a_{cc} errors in a ZnO NW bending originates from inaccurate estimations of local ε_{cc} and E_g due to the experimental setup or the ZnO plastic deformation and due to the insufficient in-plane resolution (> D), respectively.

Han X. *et al.* reported the NBE-CL peak shift of the bent NW using high energy e-beam (9 keV).[37] NWs with high aspect ratio are placed bent on underlying adhesive substrates using a manipulator in advance and its bending is maintained by the adhesive shear stress, which can be released by a drop of ethanol. They assumed that the NW bending is always elastic, that NW center is free of strain, and that a maximum local strain of NR with a diameter D is estimated to be $\varepsilon_{cc} = D/2R$ using a local curvature R^{-1}. Since then, several authors reported a_{cc} values of ZnO NW or MW by reproducing above techniques which do not match each other.[35-39,42-43] We consider the elastic strain ε_{cc} evaluated by above method is inaccurate for following reasons; (1) The circular arc approximation of local R is inaccurate due to small and ill-defined NW or MW bending; (2) NR center can be strained and the strain-neutral plane can be shifted toward the compressive region due to shear stress from the adhesive substrates; (3) The elastic strain, which shifts band-gap, may be overestimated since plastic wire deformation is not considered systematically.

Also, some publication[36-37,43] reports area-spectroscopy of a bent ZnO wire at several sections with different curvatures R^{-1}. Therein, a strain-induced bandgap shift δE_g is averaged over the e-beam scan area ranging from tensile to compressive regime of each wire section. This is often correlated with the local maximum $\varepsilon_{cc} = D/2R$ at the outer edge. Such a measurement area mismatch underestimates the reported a_{cc} values, unless free-exciton drift is prominent and free-exciton 'center of mass' reaches the wire edge : $L_{Dr} >> D$.

For above concerns, we demonstrate a high-resolution spot-CL nano-spectroscopy of a free-standing ZnO NR whose apex is loaded *in-situ* by point bending stress statically and precisely in our Nanoprobe-CL setup. The ε_{cc} distribution in a free-standing NR is well-defined and controllable for its mechanical simplicity. Nanoprobe-CL technique also enables local $E_g(\varepsilon_{ij})$ study under both tensile and compressive uniaxial strain up to the fracture strain, observation of wire plastic deformation, and evaluation of FX 'center of mass' drift in the presence of strain-gradient R^{-1}.

Supplementary Note 2

Possible mechanism of NR plastic deformation

Here, NR plastic deformation behavior which differs among NRs at $\varepsilon_{ccN,0} > 0.02$ are tentatively explained by the distribution of ZnO lattice defects within a NR and among NRs. NR plastic deformation initiates at a grown-in lattice defect around the NR bottom at which the ε_{ccN} is maximum. NR fracture takes place as a cascaded bond-cut which is observed only when the stress concentration is evident: NR bending is large and NR lattice is nearly perfect. Further *in-situ* TEM studies are required to examine this perspective.

Supplementary Note 3

a_{ccN} quench due to elastic NR bending and a_{cc} value at no strain-gradient

Correlation between NR plastic bending deformation and the a_{ccN} quench are discussed here by re-plotting Figure 3b and 3c: ($\varepsilon_{ccN,0}$, $\delta E_g(0)$) plots, ($\varepsilon_{ccN,0}$, a_{ccN}) plots, and ($\varepsilon_{ccE,0}$, a_{ccE}) plots are shown in Figure S2. We also found that the $\delta E_g(0)$ shifts down and a_{ccN} (and a_{ccE}) quenches with increasing ZnO NR bending strain $\varepsilon_{ccN,0}$ at P_0. Linear extrapolations of plots in "Elastic" regime to no bending limit (solid and dashed blue lines) give a_{ccN} = -1.73±0.14 eV and a_{ccE} = -1.71±0.14 eV where we see their offsets agree and follow equation (14). Also, both a_{ccN} and a_{ccE} quench in "Elastic" regime where the elastic deformation dominates over the plastic one. Thus, the $|a_{ccN}|$ quench is not accountable by the NR plastic deformation. We conclude a_{cc} = -1.7 eV at the no bending limit and we simply discuss the a_{ccN} quench and the negative $\delta E_g(0)$ shift due to elastic NR bending.

Supplementary Note 4

Piezo-electric field across a bent NR compensated by residual free carriers

Since a FX in ZnO has a binding energy (E_b = 0.060 eV)[7] and a Bohr radius (a_B = 1.35 nm),[44] an electric field required to dissociate a FX in ZnO is estimated.

$$F_{\mathrm{b}}\left(\mathrm{V/cm}\right)=\frac{E_b/e}{a_{\mathrm{B}}}=\frac{0.060\left(\mathrm{V}\right)}{1.35\times10^{-7}\left(\mathrm{cm}\right)}=4.4\times10^{5} \quad \text{(S1)}$$

On the other hand, piezoelectric potential at an apex of a bent NR is calculated assuming no charge compensation. Here, physical parameters are estimated using the following parameters: L = 1.4×10^{-4} cm, D = 1.5×10^{-5} cm, $\varepsilon_{ccN,0}$ = 0.01, d_{cc} = 1.24×10^{-9} cm/V, ε_{ZnO} = 2, ε_0/e = 5.526×10^5 V^{-1}cm^{-1}.

$$\begin{aligned} V_{\mathrm{Piezo}}\left(\mathrm{V}\right)&=\int_{s=0}^{L}\frac{ds\cdot\varepsilon_{ccN}\left(u,L,s,r\right)}{d_{cc}}=\frac{3ru}{2Ld_{cc}}=\frac{\varepsilon_{ccN,0}Lr}{D}\cdot\frac{1}{d_{cc}} \\ &=\left(\frac{r}{D}\right)\times1.13\times10^{3} \end{aligned} \quad \text{(S2)}$$

Under this assumption, the transverse piezo-electric field and the piezo-electric charge density at an apex of a bent NR are calculated. [equations (S3) and (S4)]

$$\begin{aligned} F_{\mathrm{Piezo}}\left(\mathrm{V/cm}\right)&=\frac{V_{\mathrm{Piezo}}\left(u,L,r\right)\big|_{r=0}^{D/2}}{D/2}=\frac{3u}{2Ld_{cc}}=\frac{\varepsilon_{ccN,0}L}{D}\cdot\frac{1}{d_{cc}} \\ &=7.53\times10^{8} \end{aligned} \quad \text{(S3)}$$

$$\begin{aligned} \sigma_{\mathrm{Piezo}}\left(\mathrm{cm}^{-2}\right)&=\frac{\varepsilon_{\mathrm{ZnO}}\varepsilon_0V_{\mathrm{Piezo}}}{eL}=\frac{3ru}{2L^2}\cdot\frac{\varepsilon_{\mathrm{ZnO}}\left(\varepsilon_0/e\right)}{d_{cc}}=\frac{\varepsilon_{ccN,0}r}{D}\cdot\frac{\varepsilon_{\mathrm{ZnO}}\left(\varepsilon_0/e\right)}{d_{cc}} \\ &=\left(\frac{r}{D}\right)\times8.91\times10^{12} \end{aligned} \quad \text{(S4)}$$

The uncompensated piezoelectric field is significantly larger than what is needed to dissociate the ZnO FX, however, such an electric field higher than the typical bulk ZnO breakdown field[45] of 2×10^6 V/cm is not maintained.

In our setup, more realistically the piezo-electric charges at NR apex are compensated *via* the contacts to the grounded ZnO substrate and W-nanoprobe indenter and by the ZnO residual carriers. The area density of the residual carriers (n_0 = 8×10^{18} cm^{-3})[58] [equation (S5)] is 2 order of magnitude larger than the piezo-electric charge. As a result, the area density of uncompensated piezoelectric charge η is nearly zero [equation (S6)].

$$\sigma_{\text{Carrier}}\left(\text{cm}^{-2}\right) = n_0 \cdot L \sim 10^{15}\left(\text{cm}^{-2}\right) \quad \text{(S5)}$$

$$\sigma_{\text{Piezo}} << \sigma_{\text{Carrier}} + \sigma_{\text{GND}} \quad \text{(S6)}$$

Thus, the piezoelectric field is significantly smaller than what is needed to dissociate the ZnO FX ($\eta F_{\text{Piezo}} < F_{\text{b}}$) or fully compensated; FXs are not dissociated during their lifetime (τ_{FX}).

Supplementary Note 5

FX 1D drift-diffusion model across a bent ZnO NR

An FX excited in a bent ZnO NR drifts under the bandgap gradient as well as it diffuses during the FX lifetime: FX drift-diffusion model. [Figure 3d] When the FX is excited by the continuous e-beam incident at the position $r_k = 0$, the FX local concentration in a bent NR, $n_{FX}(\mathbf{r})$, is described by solving the two step steady-state rate equations on hot carrier relaxation to band-edges and the FX drift-diffusion across a bent ZnO NR. [equation (S7)]

$$\begin{cases} 0 = g_0(\mathbf{r}) + D_{\text{Hot}}\nabla^2 n_{\text{Hot}}(\mathbf{r}) - \dfrac{n_{\text{Hot}}(\mathbf{r})}{\tau_{\text{Hot}}} \\ 0 = \dfrac{n_{\text{Hot}}(\mathbf{r})}{\tau_{\text{Hot}}} + D_{\text{FX}}\nabla^2 n_{\text{FX}}(\mathbf{r}) - \mu_{\text{FX}} F_{\text{g}} \cdot \nabla n_{\text{FX}}(\mathbf{r}) - \dfrac{n_{\text{FX}}(\mathbf{r})}{\tau_{\text{FX}}} \end{cases} \quad \text{(S7)}$$

Here, the first equation consists of a hot carrier generation term [equation (S8)], a ballistic diffusion term, and a loss term by the hot carrier relaxation to band-edges and the FX formation. Similarly, the second equation consists of a FX supply term, a FX diffusion term, a FX drift term, and a FX loss term by the radiative (or non-radiative) recombination.

In our previous CL study of similar ZnO NRs at primary e-beam conditions of 3 kV and 2.4 nA and at 300 K, primary e-beam size is evaluated to be σ_{PE} = 7.7 nm and CL in-plane resolution is to be 64 nm,[58] which is attributed to FX diffusion length. We adopt the following approximations.

(1) Carrier excitation profile $g_0(r)$ is approximated using $\delta(r)$ function. This is justified since primary e-beam size σ_{PE} = 7.7 nm is much smaller than dimensions of FX dynamics, FX diffusion length L_{Df} = 0.06 μm and NR diameter D = 0.15 μm.

$$g_0(r) = \frac{g_0}{\sqrt{2\pi}\sigma_{\text{PE}}} \exp\left[-\frac{r^2}{2\sigma_{\text{PE}}^2}\right] \approx g_0\delta(r) \quad \text{(S8)}$$

Carrier excitation rate g_0 is calculated using the following parameters: primary e-beam energy (E_{PE} = 3 keV), e-beam current (I_{PE} = 2.40 nA), and average ionization energy required for an electron-hole pair excitation in ZnO (E_I = 10 eV).

$$g_0 = \frac{E_{\text{PE}}}{E_{\text{I}}}\frac{I_{\text{PE}}}{e} = \frac{3000(\text{eV})}{10(\text{eV})} \cdot \frac{2.40\times10^{-9}(\text{A})}{1.60219\times10^{-19}(\text{C})} = 4.5\times10^{12}(\text{s}^{-1}) \quad \text{(S9)}$$

(2) An excited carrier pair is assumed to relax to band-edges and to form a FX instantly, since carrier relaxation (several ps) is much faster than FX lifetime (~ 1 ns).

(3) FX dynamics is assumed to be described by 1D rate equation along r axis. This is justified as long as FX dynamics is dominated by 1D FX drift rather than 3D FX diffusion. Since the impact of NR bending appears even at smallest bending curvature R^{-1} in Figure 3b, the R^{-1} region of interest is dominated by FX drift.

Under above conditions (1)-(3), equation (S7) is re-written with the FX diffusion length (L_{Df}) and the FX drift length during the FX lifetime (L_{Dr}). [equation (S10)]

$$\left[{L_{\mathrm{Df}}}^2 \nabla^2 - L_{\mathrm{Dr}} \cdot \nabla - 1 \right] \cdot n_{\mathrm{FX}}(r) = -g_0 \tau_{\mathrm{FX}} \cdot \delta(r) \qquad \text{(S10)}$$

$$L_{\mathrm{Df}} \equiv \sqrt{D_{\mathrm{FX}} \tau_{\mathrm{FX}}} = 0.06(\mu\mathrm{m}) \qquad \text{(S11)}$$

$$L_{\mathrm{Dr}} \equiv \mu_{\mathrm{FX}} \tau_{\mathrm{FX}} F_{\mathrm{g}} = \frac{|a_{cc}| \mu_{\mathrm{FX}} \tau_{\mathrm{FX}}}{R} \qquad \text{(S12)}$$

(4) We define the FX distribution $n_{\mathrm{FX}}(r)$ at r = [0, $+\infty$], the region of interest for numerical simplicity and generality over various dimensions of D. We may assume that the $n_{\mathrm{FX}}(r)$ is not affected by FX accumulation at the NR outer edge and FX surface recombination rate is constant anywhere in the NR. They are justified since FX drift parameter $\mu_{\mathrm{FX}}\tau_{\mathrm{FX}}$ is determined by the initial $|a_{cc}(R^{-1})|$ decrease with small R^{-1} in Figure 3b and since the 3 keV PE beam excites FXs at the surface vicinity which are subject to surface recombination. Thus, the $n_{\mathrm{FX}}(r)$ decays with r and is normalized by steady state FX population. [equation (S13)]

$$\begin{cases} n_{\mathrm{FX}}(r \to \infty) = 0 \\ \int_0^{\infty} dr \cdot n_{\mathrm{FX}}(r) \equiv g_0 \tau_{\mathrm{FX}} \end{cases} \qquad \text{(S13)}$$

The solution of 1D rate-equation (S10) is normalized under equation (S13), which is written as equation (S14) using $L_{\mathrm{Dr\text{-}Df}}$ in equation (S15).

$$n_{\mathrm{FX}}(r) = \frac{g_0 \tau_{\mathrm{FX}}}{L_{\mathrm{Dr\text{-}Df}}} \cdot \exp\left[-\frac{r}{L_{\mathrm{Dr\text{-}Df}}} \right] \qquad \text{(S14)}$$

$$L_{\mathrm{Dr\text{-}Df}} = \frac{L_{\mathrm{Df}}}{\sqrt{1 + \left(\frac{L_{\mathrm{Dr}}}{2L_{\mathrm{Df}}} \right)^2} - \frac{L_{\mathrm{Dr}}}{2L_{\mathrm{Df}}}} \qquad \text{(S15)}$$

Considering the FX travel by the drift and the diffusion from primary e-beam position $r_k = 0$, a statistical FX travel distance, $\langle L_{\mathrm{Dr\text{-}Df}} \rangle (r_k = 0)$, is deduced by averaging each FX travel distance over r =

[0, +∞] with the weight $n_{FX}(r)$, which is r inside the NR ($0 < r < D/2$) and $D/2$ at the NR outer edge ($r > D/2$). Then we obtain $\langle L_{Dr\text{-}Df}\rangle(r_k)$ by replacing $D/2$ by $D/2\text{-}r_k$ in equation (S16).

$$\left\langle L_{Dr\text{-}Df}\right\rangle\left(r_k=0\right)=\frac{\int_0^{D/2}dr\cdot n_{FX}\left(r\right)\cdot r+\int_{D/2}^{\infty}dr\cdot n_{FX}\left(r\right)\cdot\frac{D}{2}}{\int_0^{\infty}dr\cdot n_{FX}\left(r\right)}=\frac{D}{2}\cdot\left[\frac{1-\exp\left(-\frac{D/2}{L_{Dr\text{-}Df}}\right)}{\frac{D/2}{L_{Dr\text{-}Df}}}\right]$$

$$\xrightarrow{D/2\rightarrow D/2-r_k}\left\langle L_{Dr\text{-}Df}\right\rangle\left(r_k\right)=\left(D/2-r_k\right)\cdot\left[\frac{1-\exp\left(-\frac{D/2-r_k}{L_{Dr\text{-}Df}}\right)}{\frac{D/2-r_k}{L_{Dr\text{-}Df}}}\right]$$

Since the $\langle L_{Dr\text{-}Df}\rangle(r_k)$ is not significantly affected by the 3D FX diffusion even when the FX diffusion is dominant, it is further approximated by $L_{Df} = 0$ to be $\langle L_{Dr}\rangle(r_k)$, which is valid for whole range of R^{-1} = [0, +∞].

$$\xrightarrow{L_{Df}\rightarrow 0}\left\langle L_{Dr}\right\rangle\left(r_k\right)=\left(D/2-r_k\right)\cdot\left[\frac{1-\exp\left(-\frac{D/2-r_k}{L_{Dr}}\right)}{\frac{D/2-r_k}{L_{Dr}}}\right]\quad\text{(S16)}$$

A series of **spot-CL spectroscopy** observes the a_{ccN} quench in Figure 3b and the $\delta E_g(0)$ redshift in Figure 3c with increasing NR local curvature R^{-1}. The FX excited in the region $r_k = [D/2\text{-}\langle L_{Dr}\rangle(r_k), D/2]$ has no contribution to the a_{ccN}. Thus, the $a_{cc}(R^{-1})$ is expressed by averaging local contribution $a_{cc}\cdot[1 - \langle L_{Dr}\rangle(r_k)/(D/2\text{-}r_k)]$ over the range of $r_k = [-\Delta/2, +\Delta/2]$. [equation (S17)] Here, Δ (< D) is the width of measurement spot distribution. This $a_{cc}(R^{-1})$ is a fit function in Figure 3b to determine the FX drift parameter, $\mu_{FX}\tau_{FX}$. Here, we further formulated $a_{cc}(R^{-1})$ approximations at two limits ($R^{-1} \rightarrow 0$ and $R^{-1} \rightarrow +\infty$), which justifies a linear extrapolation of (R^{-1}, a_{ccN}) plots at $R^{-1} \rightarrow 0$ to evaluate a_{cc} = -1.7 eV [or ($\varepsilon_{ccN,0}$, a_{ccN}) plots at $\varepsilon_{ccN,0} \rightarrow 0$ as is done in Figure S2b].

$$a_{cc}\left(R^{-1}\right)=a_{cc}\cdot\left[\frac{1}{\Delta}\int_{-\Delta/2}^{+\Delta/2}dr_k\cdot\left\{1-\frac{\left\langle L_{Dr}\right\rangle\left(r_k\right)}{D/2-r_k}\right\}\right]=a_{cc}\cdot\left[1-\frac{L_{Dr}}{\Delta}\cdot\left\{\int_{\frac{D-\Delta}{2L_{Dr}}}^{\frac{D+\Delta}{2L_{Dr}}}dv\cdot\frac{1-e^{-v}}{v}\right\}\right]$$

$$\xrightarrow{\Delta\to 0} a_{cc}\cdot\left[1-\left\{\frac{1-\exp\left(-\frac{D/2}{L_{\mathrm{Dr}}}\right)}{\frac{D/2}{L_{\mathrm{Dr}}}}\right\}\right]=a_{cc}\cdot\left[1-\left\{\frac{1-\exp\left(-\frac{D/2}{|a_{cc}|\mu_{\mathrm{FX}}\tau_{\mathrm{FX}}R^{-1}}\right)}{\frac{D/2}{|a_{cc}|\mu_{\mathrm{FX}}\tau_{\mathrm{FX}}R^{-1}}}\right\}\right] \quad \text{(S17)}$$

$$\approx\begin{cases} a_{cc}\cdot\left(1-\dfrac{|a_{cc}|\mu_{\mathrm{FX}}\tau_{\mathrm{FX}}}{D/2}\cdot R^{-1}\right) & \left[R^{-1}\to 0\right] \\ \dfrac{a_{cc}}{2}\cdot\left(\dfrac{|a_{cc}|\mu_{\mathrm{FX}}\tau_{\mathrm{FX}}}{D/2}\cdot R^{-1}\right)^{-1} & \left[R^{-1}\to\infty\right] \end{cases}$$

Contrary, the FX drift excited at $r_k = 0$ is the origin of the $\delta E_g(0)$ redshift. Thus, the $[\delta E_g(0)](R^{-1})$ is also formulated. [equation (S18)] This $[\delta E_g(0)](R^{-1})$ is a fit function in Figure 3c to describe the $\delta E_g(0)$ redshift by the FX drift-diffusion model.

$$\left[\delta E_g\left(0\right)\right]\left(R^{-1}\right)\propto a_{cc}\cdot\left\langle L_{\mathrm{Dr}}\right\rangle\left(r_k=0\right)=a_{cc}\cdot\frac{D}{2}\cdot\left[\frac{1-\exp\left(-\frac{D/2}{|a_{cc}|\mu_{\mathrm{FX}}\tau_{\mathrm{FX}}R^{-1}}\right)}{\frac{D/2}{|a_{cc}|\mu_{\mathrm{FX}}\tau_{\mathrm{FX}}R^{-1}}}\right] \quad \text{(S18)}$$

Supplementary Note 6

Room temperature spot-CL spectroscopy of a typical ZnO NR without bending

A SEM image of ZnO NRs are shown from side-view angle. [Figure S4a] A local position (*s*, *r*) on a NR array from a side-view angle is defined and classified into 3 regions: "above PMMA", "in PMMA", and "Sub." for Spot-CL baseline study. A corresponding room temperature NBE CL image indicates that NBE CL intensity "above PMMA" increases from NR apex toward NR bottom and is rather uniform across NR axis. [Figure S4b] Room-temperature area-CL spectra from side-view angle exhibits NBE CL peak at 3.27 eV and red emission band at around 2.1 eV. [Figure S4c] The E_{FX} is a FX CL peak energy obtained by a spot-CL spectroscopy on a ZnO NR at room temperature and determined by Gaussian curve fitting of CL peak within its FWHM. Here, spatial distribution of FX CL peak energy on a typical unbent ZnO NR (E_{FX}^{0}) is rigorously investigated beforehand at room temperature. [Figure S4] Obtained E_{FX}^{0} redshifts gradually from the NR apex toward its bottom "Above PMMA", while it is uniform across the NR axis. [Figures S4d and S4e] The 6 plots "Above PMMA" (s > 300 nm) are fitted with a linear function at L = 1468 nm (dashed black line).

$$E_{FX}^{0}(\mathrm{eV}) = 3.281 - 2.161\times10^{-5}\cdot\{L(\mathrm{nm}) - s(\mathrm{nm})\} \quad \text{(S19)}$$

The E_{FX}^{0} behavior observed in Figure S4d is attributed to the bi-directional NR growth: axial (+c) and lateral (m) growths which are illustrated with dark and light grey colors, respectively. NR lateral growth thickness increases with (L-s), which is roughly proportional to the lateral growth duration under constant growth rate approximation. However, NR lateral growth is prohibited at NR bottom (s < 300 nm) due to the coverage of 300 nm-thick PMMA film.

Our previous study accounts for FX emission energy redshift due to high carrier concentration; NR lateral growth incorporates donors at higher rate than NR axial growth which induces a band-tailing or a band-gap shrinkage in ZnO.[58] As a result, the FX emission energy at NR lateral growth domain is lower than 3.28 eV at NR axial growth domain. In this room-temperature spot-CL study, the emerging contribution of NR axial growth domain with (L-s) is treated as a E_{FX}^{0} redshift and the broadening of a single Gaussian peak, since the two possible emission bands at NR core and shell are unresolved and observed as increased FWHMs "above PMMA". The line-fitting offset $E_{FX}^{0}(0)$ = 3.281 eV agrees with our previous observation in NR axial growth domain. The E_{FX}^{0} redshifts linearly and NBE-CL intensity increases with (L-s) "above PMMA", which is accounted by the fraction of NR lateral growth domain in the CL probe regime. In this study, NR lateral growth domain thickness is reduced to t_m = 5±2 nm. The a_{ccN} measurements are performed at around s ~ 400 nm so that NBE-CL signal at E_{PE} = 3 keV is

dominantly emitted from the NR lateral growth domain but the diameter gap does not degrade local ε_{ccN} evaluation.

Supplementary Note 7

Liquid N_2 temperature area-CL studies of a ZnO NR under a bending deformation cycle

Area-CL spectroscopy of ZnO NR under bending is also performed at liquid N_2 temperature to demonstrate validity of this technique at low temperature. [Figure S5] To obtain a sharp NBE CL emission line, ZnO NR array is cooled down by N_2 gas flow in the cryostat specimen stage at T_{Stage} = 80 K. A NR bending deformation cycle is shown in a sequence of SEM images, where a ZnO NR is under "Probe contact", loaded by "Bending", and unloaded by "Probe retract", respectively. [Figure S5a] Note that this NR bending deformation is elastic since it returns to original position after "probe retract" step ($u' \sim 0$). Area-CL spectroscopy is performed at each step. Nominal uniaxial strain in this NR bending is $\varepsilon_{ccN,0}$ = 0.029 at P_0 and $\varepsilon_{ccN,s}$ = 0.014 at P_s. Corresponding area CL spectra at both "probe-contact" and "bending" steps exhibit free exciton peaks (FX_A), their LO phonon replicas (FX_A–mLO : m = 0, 1, 2, 3), and neutral donor-bound exciton peaks (D^0X_A). [Figure S5b] All peak widths broaden by the NR bending but their notable energy shifts are not observed.

To evaluate this CL peak broadening under the reduced the fitting parameters, each CL spectrum is fitted with 5 Lorentzian peaks under the constraints that energies of four FX_A–mLO peaks follow their reported T-dependences.[S1] [Figure S5c] The temperature dependent bandgap including lattice dilation effects and electron-phonon coupling is denoted as equation (S20).

$$E_{FX_A}(T) = E_{FX_A}(0) - UT - \frac{\alpha\theta}{\exp(\theta/T)-1} \quad \text{(S20)}$$

Here, we adopted the following parameters in reference S1: bandgap at 0 K: E_{FX} (0) = 3.3761 (eV), lattice dilation constant U = 5×10^{-5} (eV/K), effective exciton-phonon coupling strength: α = 5×10^{-4} (eV/K), and effective phonon temperature: θ = 370 (K). The energy interspacing of FX_A-mLO peaks are denoted as equation (S21). We also adopted LO phonon energy $\hbar\omega_{LO}$ = 0.072 (eV) and coefficient of exciton kinetic energy: L = 1 (m = 1) or 0 (m = 2, 3).

$$E_{FX_A\text{-}m\text{LO}}(T) = E_{FX_A}(T) - m\cdot\hbar\omega_{LO} + \left(L+\frac{1}{2}\right)k_BT \quad \text{(S21)}$$

This fitting evaluates the temperature of a NR under W-probe contact (T_{NR} = 120±5 K) and D^0X_A peak energies (3.342±0.001 eV) and their differences by the NR bending are within their error ranges. ZnO (0001) substrate temperature is also evaluated by T-dependent CL spectroscopy at the bottom of the same NR (T_{Sub} = 110±5 K). [Figure S5d] Note that the NR is not thermalized by a W-nanoprobe contact even when the W-nanoprobe is at room temperature. [Figure S5e] This is

explained by their heat conductance gap between NR bottom and W-nanoprobe contact.

The FWHM broadening of all peaks fitted to NR CL spectra are summarized in Supplementary Table 1. Two major CL peaks (D^0X_A and FX_A-1LO) exhibit their FWHM broadening (ΔFWHM ~ 6 meV) due to the bending strain ($\varepsilon_{ccN,s}$ = 0.014): ΔFWHM/$\varepsilon_{ccN,s}$ ~ 0.4 eV. Considering graded bandgap shifts, negative in tensile regime and positive in compressive regime, above results suggest that the deformation potential (a_{cc}) should be of the order of 1 eV at liquid N_2 temperature, as well.

Also, the impact of NR bending on the LO phonon coupling behavior is investigated. The FX_A–mLO peak intensity, I_m, is plotted as a function of m, which exhibits an exponential intensity decrease. [Figure S5f] The LO phonon coupling is evaluated by a Huang-Rhys factor S which describes the average number of optical phonons excited in the transition.

$$\frac{I_m}{I_0} = \frac{S^m}{m!}\exp(-S) \qquad (m = 1, 2, 3\ldots) \qquad \text{(S22)}$$

The S is determined on each CL spectrum by fitting the CL intensity decay of LO phonon replica with $m \geq 1$, since the zero phonon (m = 0) emission band overlaps several other recombination bands. Both "Probe contact" and "Bending" CL spectra exhibits a similar exponential decay (S_0 = 0.33±0.01 and S_ε = 0.40±0.03, respectively) which is slower than that of the hydrothermally grown ZnO substrate (S_{Sub} = 0.23±0.01). This implies that the NR bending might strengthen the LO phonon coupling, however, such a change is smaller than that due to the growth method difference which differs the degree of ZnO crystallinity.

Above results obtained at liquid N_2 temperature demonstrates a wide-range applicability of Nanoprobe-CL technique to indirect-gap materials (*e.g.* Si, Ge), which is less-luminescent than ZnO at room temperature.

REFERENCES

S1. Mendelsberg, R. J.; Allen, M. W.; Durbin, M.; Reeves, R. J. Photoluminescence and the Exciton Phonon Coupling in Hydrothermally Grown ZnO. *Phys. Rev. B* **2011**, 83, 205202.

Supplementary Table 1

Area-CL peak broadening due to the NR bending

The FWHM broadening of all peaks fitted to NR CL spectra are summarized in Supplementary Table 1. The reliable *Δ*FWHM values are indicated with thick letters, which are significantly larger than their root-mean-square errors.

CL peak	FX_A	D^0X_A	FX_A–1LO	FX_A–2LO	FX_A–3LO
Peak energy (eV) at 120 K	3.3620	3.342	3.3055	3.2232	3.1512
FWHM (meV) in “probe-contact”	8.5±10.5	25.0±3.9	54.7±2.1	43.8±7.5	27.5±37.0
FWHM (meV) in “bending”	13.3±9.1	31.3±3.4	60.4±2.4	61.7±11.4	28.7±41.1
*Δ*FWHM (meV)	+4.9	**+6.3**	**+5.7**	+17.9	+1.2

Supplementary Figure S1

Spot-CL spectroscopy across a largely bent ZnO NR and NR plastic deformation

(A) Side-view (*m* axis) SEM images of a ZnO NR before bending ($\varepsilon_{ccN,0}$ = 0 at P_0), under large bending ($\varepsilon_{ccN,0}$ = 0.050 at P_0 in Run 1 and $\varepsilon_{ccN,0}$ = 0.061 at P_0 in Run 2), and after the bending ($\varepsilon_{ccP,0}$ = 0.032 at P_0). A plastic deformation is observed due to the stress concentration at the vicinity of the NR bottom, indicated by a green arrow. Spot-CL spectroscopy is performed on this NR under large bending (N = 5 in any Run). (B) Obtained CL spectra in Run 2. (C) The (ε_{ccN}, δE_g) plots in Runs 1 and 2. All panels are displayed in the same manner as Figure 1.

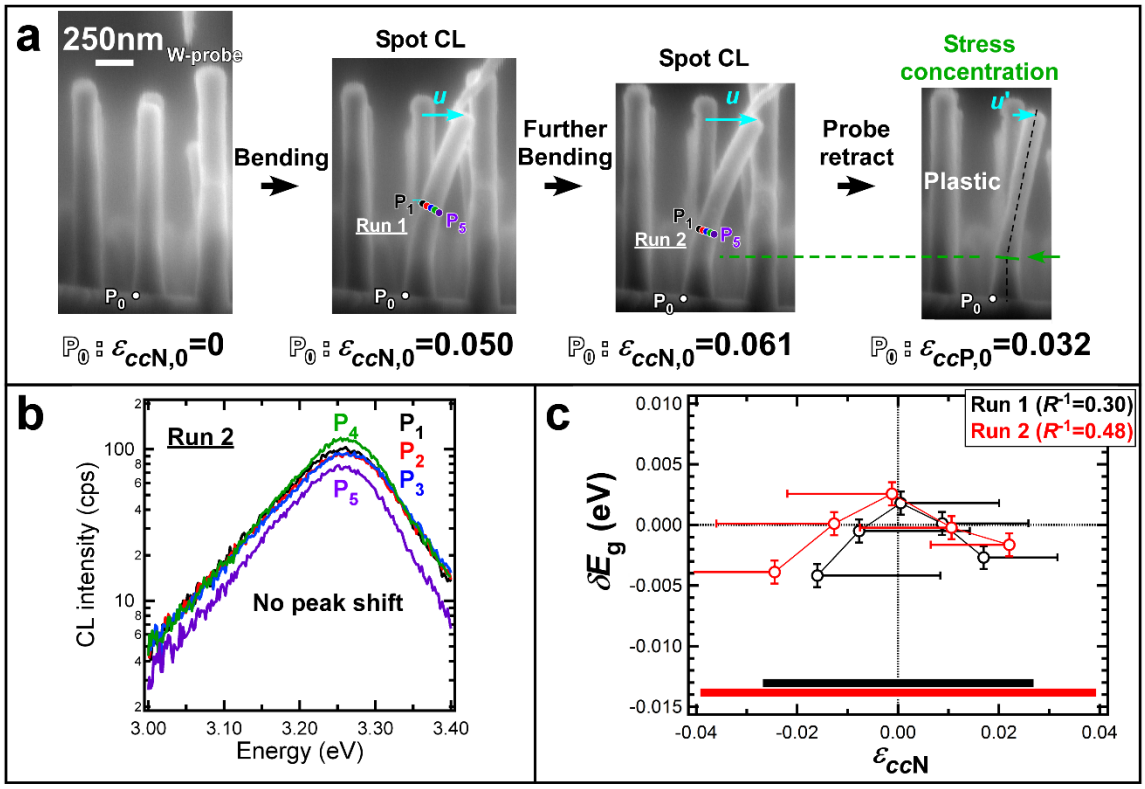

Supplementary Figure S2

Statistical correlation between NR bending magnitude and nominal a_{ccN} and $\delta E_g(0)$

(A) The ($\varepsilon_{ccN,0}$, $\delta E_g(0)$) plots indicating the $\delta E_g(0)$ shift due to the NR bending. A negative $\delta E_g(0)$ shift of up to about -0.007 eV is observed. (B) The ($\varepsilon_{ccN,0}$, a_{ccN}) plots indicating the "as-observed" bandgap deformation potential at each NR bending. (C) The ($\varepsilon_{ccE,0}$, a_{ccE}) plots indicating the bandgap deformation potential quenching due to each *elastic* NR bending. The $\varepsilon_{ccE,0}$ and a_{ccE} are calculated using equation (??). The error bars are determined in the same manner as Figure 3. "Elastic" and "Plastic" deformation regimes of $\varepsilon_{ccN,0}$ are highlighted in panels (A) and (B).

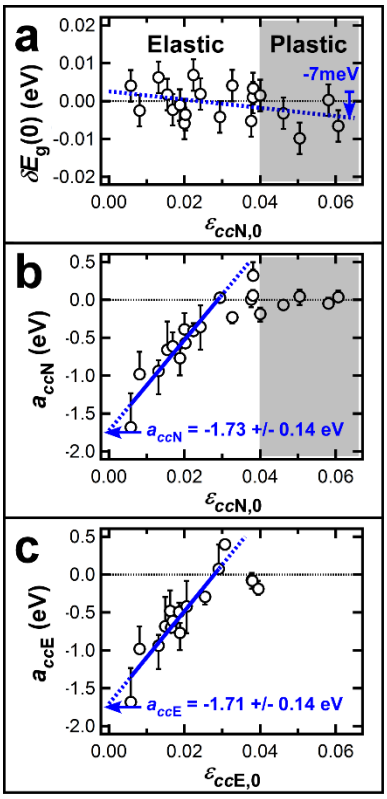

Supplementary Figure S3

Reported bandgap deformation potentials a_P of ZnO under hydrostatic pressure

(A) The ($V^{-1/3}$, a_P) plots. (B) The ($1/R_{Exc}$, a_P) plots. The measurement plot based on the 2*hv*-PA spectroscopy[10] is omitted from panel (B). All panels are displayed in the same manner as Figure 4.

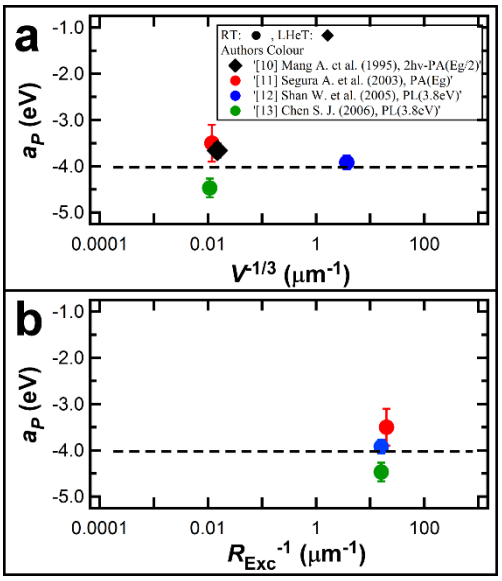

Supplementary Figure S4

Room temperature spot-CL spectroscopy of a typical ZnO NR without bending

(A) A side-view (*m* axis) SEM image of a ZnO NR array. A coordinate (*s*, *r*) of a spot CL spectroscopy are indicated and the measurement positions of spot-CL spectroscopy are categorized into 3 regions highlighted with different grey contrasts: “Above PMMA”, “In PMMA”, and “Sub.”. (B) A corresponding NBE CL image (E = 3.27 eV). (C) Area CL spectrum of a ZnO NR array recorded from the side-view angle (*m* axis) exhibiting a FX_A emission line at 3.27 eV and a red emission band at 2.1 eV. (D) NBE CL peak intensity, energy (black), and FWHM (red) plotted as a function of *s* at r = 0 nm. The 6 plots on a NR (L=1468 nm) “Above PMMA” are fitted with a linear function $E_{FX}(L\text{-}s) = 3.281\text{-}2.161\times10^{-5}\cdot(L\text{-}s)$ (dashed black line). The inset shows a cross-sectional schematic of a ZnO NR on a ZnO (0001) substrate from a side view (*a* axis). The domain of ZnO NR axial (+*c*) and lateral (*m*) growths are indicated with dark and light grey colors, respectively. The CL probe depth (R_{KO} = 98 nm) is also illustrated as a red ellipsoid on a ZnO NR. (E) NBE CL peak intensity, energy (black), and FWHM (red) plotted as a function of *r* at *s* = 600 nm. The inset shows a cross-sectional schematic of a ZnO NR and CL probe depth from a top view (*c*-axis).

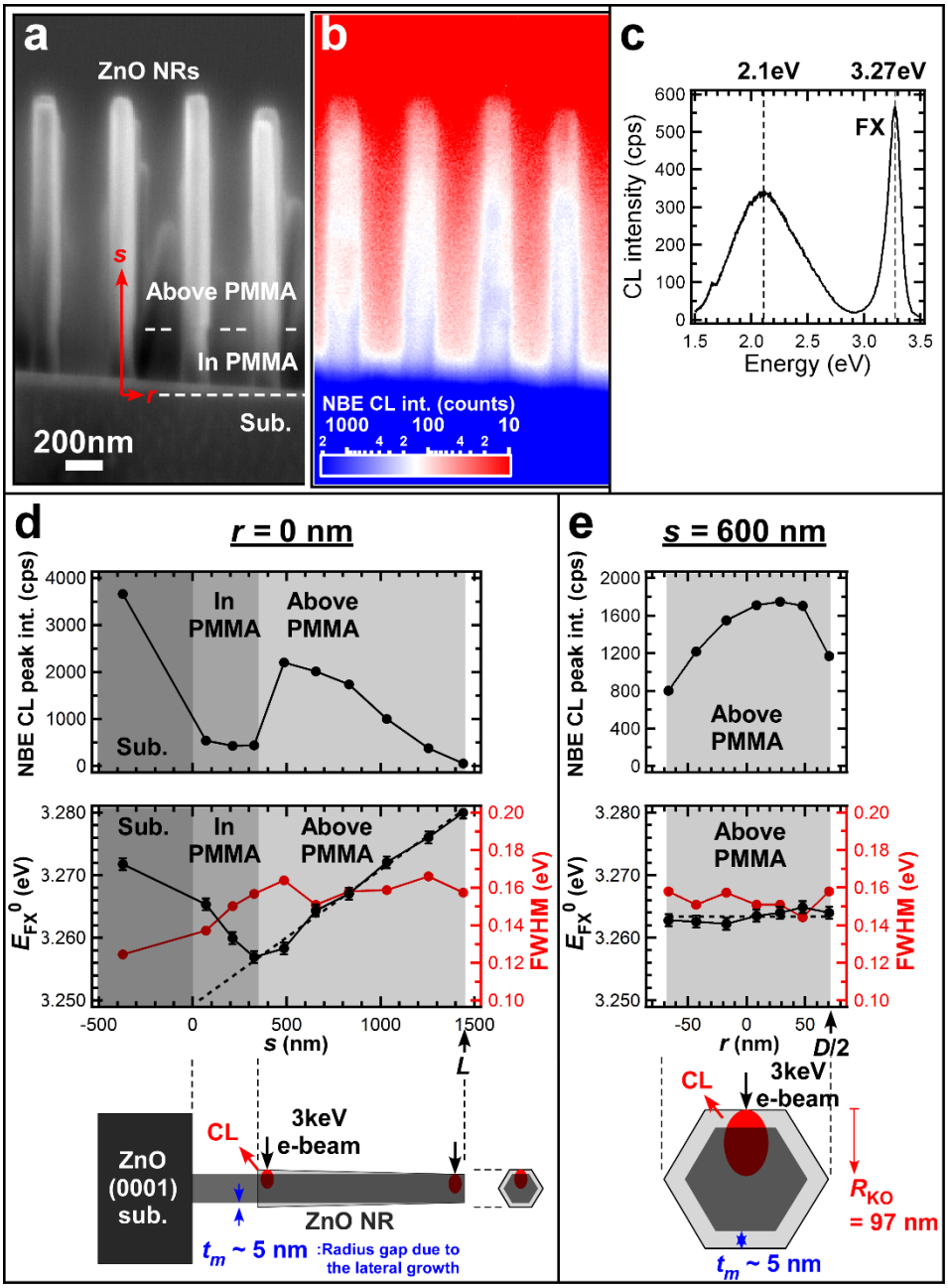

Supplementary Figure S4

Supplementary Figure S5

Liquid N_2 temperature area-CL studies of a ZnO NR under a bending deformation cycle

(A) A series of side-view (*m* axis) SEM images of a ZnO NR before bending ("Probe contact", $\varepsilon_{ccN,0} = 0$ at P_0), under small bending ("Bending", $\varepsilon_{ccN,0} = 0.029$ at P_0), and after the bending ("Probe retract", $\varepsilon_{ccP,0} \approx 0$ at P_0). White empty boxes indicate the electron beam scan areas of area-CL spectroscopies. Maximum ε_{ccN} averaged in the measurement area in "Bending" is represented by $\varepsilon_{ccN,s} = 0.014$ at P_s. (B) Area-CL spectra obtained at "Probe contact" (black) and "Bending" (red) steps at liquid N_2 temperature ($T_{Stage} = 80$ K). Each peak is assigned to either FX_A-m·LO (LO phonon replica number, $m = 0, 1, 2, 3$) or D^0X_A. (C) The curve fitting of NR area-CL spectra (dashed line) by 5 Lorentzian emission lines at $T_{NR} \sim 120$ K (solid lines). All Lorentzian peaks exhibit their FWHM broadening after the NR bending but do not exhibit their peak energy shifts. (D) A CL spectrum at the cross-section of ZnO (0001) substrate beneath the NR. It is fitted by 5 Lorentzian emission lines at $T_{Sub} \sim 110$ K in the same way. (E) A schematic of a free-standing ZnO NR under liquid N_2 cooling and W-probe contact. Evaluated local temperatures are also noted. (F) Each CL peak intensity in panels (C) or (D) plotted as a function of LO phonon number *m*. Corresponding Huang-Rhys factor *S* of each CL spectrum is also noted.

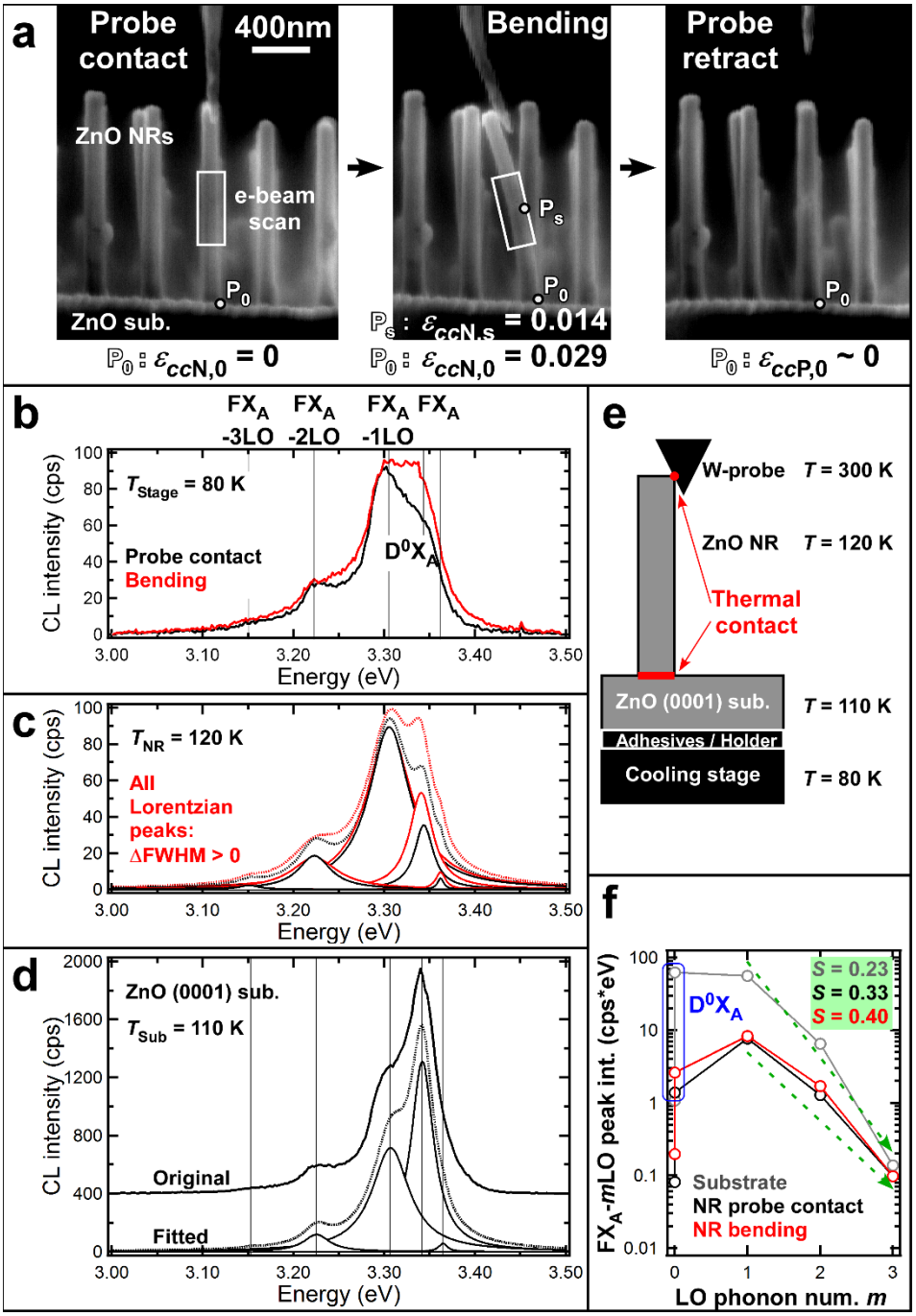

Supplementary Figure S5